

1 Introducing LAB60: A $1/60^\circ$ NEMO 3.6 numerical simulation of the Labrador Sea

2 Clark Pennelly^{1*} and Paul G. Myers¹

3 ¹1-26 Earth Sciences Building, University of Alberta, Edmonton, Alberta, Canada, T6G 2E3

4 *Correspondence to: Clark Pennelly (pennelly@ualberta.ca)

5
6 Abstract

7 A high-resolution coupled ocean-sea ice model is set up within the Labrador Sea. With a
8 horizontal resolution of $1/60^\circ$, this simulation is capable of resolving the multitude of eddies
9 which transport heat and freshwater into the interior of the Labrador Sea. These fluxes strongly
10 govern the overall stratification, deep convection, restratification, and production of Labrador
11 Sea Water. Our regional configuration, spanning the full North Atlantic and Arctic, includes
12 nested domains within the North Atlantic and Labrador Sea, reducing computational costs that
13 allow for a lengthy simulation from 2002 to the near-present time. Three passive tracers are
14 also included: Greenland runoff, Labrador Sea Water produced during convection, and Irminger
15 Water which enters the Labrador Sea along Greenland. We describe the configuration setup
16 and compare against similarly forced lower-resolution simulations to better describe how
17 horizontal resolution impacts the representation of the Labrador Sea in the model.

18
19 1. Introduction

20 The Labrador Sea, between Canada and Greenland, plays a crucial role in the climate
21 system. Situated between the Canadian Arctic and the North Atlantic, multiple current systems
22 influence this deep basin. Cold and fresh Arctic water flows south through Fram Strait along
23 Greenland (de Steur et al., 2009), producing the East Greenland Current (EGC). The EGC flows to
24 the southern tip of Greenland, merging with warm and salty Irminger Water to become the
25 West Greenland Current (WGC) before flowing northwards along the western coast (Fratantoni
26 and Pickart, 2007). The WGC flows cyclonically around the Labrador Sea as well as into Baffin
27 Bay. Significant amounts of freshwater are supplied to this current system from both Davis
28 (Cuny et al., 2005; Curry et al., 2011; Curry et al., 2014) and Hudson Strait (Straneo and Saucier,
29 2008) as it travels around the Labrador Sea. The current system is called the Labrador Current

30 where it merges with the outflow from Hudson Strait (Lazier and Wright, 1993). The Labrador
31 Current travels southwards along the eastern coast of North America eventually leaving the
32 Labrador Sea.

33 Numerous eddies are generated throughout the Labrador Sea, both from high lateral
34 density gradients which exist during the convection season (Frajka-Williams et al., 2014) as well
35 as from baroclinic and barotropic instabilities that occur within the boundary currents (Chanut
36 et al., 2008; Gelderloos et al., 2011). The continental slope along the west coast of Greenland
37 has a pronounced change in topography that induces instability of the current system,
38 generating eddies (de Jong et al., 2016). These eddies, known as Irminger Rings, contain a
39 significant amount of freshwater at the surface as well as subsurface heat. Irminger Rings (15-
40 30km radius) typically travel southwestwards into the interior of the Labrador Sea and have a
41 lifespan of up to two years (Lilly et al., 2003). Eddies generated along the Labrador Coast also
42 contain a significant amount of freshwater (Schmidt and Send, 2007; McGeehan and
43 Maslowski, 2011; Pennelly et al., 2019). Regardless of where they are produced, these
44 boundary current eddies often export their properties towards the centre of the basin (Pennelly
45 et al., 2019), influencing the deep convection which occurs. Convective eddies are generated
46 from baroclinic instability which arises from large horizontal density gradients during the
47 convective season (Marshall and Schott, 1999). Convective eddies are much smaller with a
48 radius between 5 and 18 km (Lilly et al., 2003). These eddies are less studied than the other
49 eddy types, partly due to a lack of observations (Lilly et al., 2003) as well as their small size
50 which requires high-resolution models to adequately resolve. Research into the role of each of
51 the above eddies and their role in restratifying the Labrador Sea is still ongoing; there is no
52 consensus on which eddy may be more important, though many have narrowed it down to
53 Irminger Rings and convective eddies (Chanut et al., 2008; Gelderloos et al., 2011; Rieck et al.,
54 2019).

55 Deep convection is a rather rare occurrence, only known to occur at a few places in the
56 ocean. The reason so few places exist is the stringent criteria to produce deep convection: weak
57 stratification that can be enhanced via isopycnal doming as a result of cyclonic circulation, and
58 intense air-sea buoyancy loss (Lab Sea Group, 1998; Marshall and Schott, 1999). Cyclonic

59 circulation and the lateral input of salty Irminger Water helps keep the Labrador Sea weakly
60 stratified. Furthermore, the Labrador Sea experiences strong heat loss during the winter period
61 due to the very cold mid-latitude cyclones which frequent the region (Schulze et al., 2016). The
62 overlying cold and dry air forces a significant flux of heat from the ocean to the atmosphere.
63 This loss of heat promotes the surface layer to increase in density, overturning the weakly
64 stratified water column such that the mixed layer can exceed 2000m in depth (Yashayaev,
65 2007), producing a thick uniform water mass known as Labrador Sea Water (LSW).

66 Once the convective winter ends, the Labrador Sea quickly restratifies itself within 2-3
67 months (Lilly et al., 1999), primarily due to large horizontal density gradients that form
68 convective eddies (Lilly et al., 2003; Rieck et al., 2019) as a result of the deep convection period
69 (Frajka-Williams et al., 2014). The boundary currents continuously shed eddies with relatively
70 buoyant water towards the interior Labrador Sea (Straneo, 2006), increasing stratification. This
71 occurs along the west Greenland and Labrador coasts, though research suggests that the
72 former supplies more freshwater (Myers, 2005; Schmidt and Send, 2007; McGeehan and
73 Maslowski, 2011; Pennelly et al., 2019).

74 LSW is exported out of the Labrador Sea primarily by the Deep Western Boundary
75 Current (Kieke et al., 2009), though it also spreads eastwards at a slower rate. While LSW is the
76 lightest component within the Deep Western Boundary Current, it is one of the water masses
77 which make up the lower limb of the Atlantic Meridional Overturning Circulation (AMOC). As
78 the overturning circulation transports a significant amount of heat and dissolved gasses
79 between the equator and polar regions, changes in the production of deepwater can influence
80 the overturning circulation and ultimately the climate (Bryden et al., 2005). With polar
81 amplification driven by the positive ice-albedo feedback loop, additional freshwater from
82 melted ice enters the EGC and WGC (Bamber et al., 2012). The Labrador Sea is experiencing an
83 increase in freshwater that can be capable of capping convection and preventing LSW from
84 being formed, ultimately reducing the AMOC strength (Böning et al., 2016). However, a non-
85 local increase in the surface freshwater flux may promote AMOC strengthening (Cael and
86 Jansen, 2020) or compensate the local effects of additional freshwater (Latif et al., 2000). Long
87 climate simulations allow investigation into any AMOC regime shifts that shorter, higher-

88 resolution simulations may miss. With such different conclusions, freshwater's influence on the
89 AMOC is not fully known and may vary at different convection regions.

90 While satellite altimetry provides a wealth of information including sea surface height
91 anomalies, geostrophic currents, and waves, hydrographic cruises within the Labrador Sea are
92 often limited to the restratification period when the Labrador Sea is more hospitable for
93 scientific operations. Argo floats, autonomous drifting profilers which can sample down to
94 2000m, have become a popular instrument to acquire in-situ data. However, they still lack
95 coverage within the Labrador Sea which can experience deep convection below their sampling
96 depth (Yashayaev, 2007). Numerical modelling is a useful tool to explore this data-sparse
97 region, though it has its limits. Simulations within the Labrador Sea often experience a drift in
98 model data, producing a Labrador Sea which slowly increases in salinity, and thus density
99 (Treguier et al., 2005; Rattan et al., 2010). Coarse-resolution simulations suffer even further,
100 often overproducing the spatial area of deep convection (Courtois et al., 2017), primarily as a
101 result of not resolving important small-scale features including eddies. These eddies supply the
102 Labrador Sea with significant heat (Gelderloos et al., 2011) and freshwater fluxes (Hátún et al.,
103 2007), both strongly impact the stratification, convection, and production of deep water.
104 Increased horizontal resolution helps produce these eddies and their important fluxes into the
105 interior of the Labrador Sea but numerical drift still is present within high-resolution
106 simulations, albeit reduced in severity (Marzocchi et al., 2015).

107 Numerous high-resolution simulations have been carried out within the North Atlantic.
108 VIKING20X (Rieck et al., 2019), and its predecessor VIKING20, are global $1/4^\circ$ simulations which
109 have a high-resolution $1/20^\circ$ nest. VIKING20X is a multi-decade simulation which is capable of
110 resolving eddies within the Labrador Sea. However, simulations with $1/20^\circ$ horizontal resolution
111 may not resolve sub-mesoscale processes (Su et al., 2018) that can impact stratification by
112 carrying heat and freshwater; higher-resolution is needed. The $1/50^\circ$ HYCOM (Chassignet and
113 Xu, 2017), $1/60^\circ$ NATL60 (Fresnay et al., 2018) and eNATL60 (Le Sommer et al., in prep) provide
114 great insights on the importance of resolving eddies. However, computational expense with
115 such high-resolution simulations is very high, both in computer time and operational costs. This
116 often forces higher-resolution simulations to have a reduced length, perhaps only a few years.

117 The Labrador Sea experiences significant interannual variability (Fischer et al., 2010) and such
118 short simulations may completely miss any connection between LSW production and changes
119 in the AMOC. As such, any high-resolution simulation which is capable of resolving the fine
120 scale features within the Labrador Sea should be carried out for many years to further
121 understand the climate system. Resolving the full North Atlantic at high resolution ($1/60^\circ$) and
122 carrying out a simulation for longer than 10 years would currently be extremely expensive; the
123 above $1/60^\circ$ simulations are 5 or so years in length. However, one can incorporate nested
124 domains to increase horizontal resolution with a relatively minor increase in computing cost.

125 To simulate the Labrador Sea as accurately as possible, we set up a complex numerical
126 configuration which achieves very high resolution within the Labrador Sea while keeping
127 computing costs low such that we will produce over 15 years of simulated data. This simulation
128 will be kept up to near-present time, lagged a few months depending on the availability of
129 forcing data. The high resolution allows for explicit representation of eddies which are crucial to
130 controlling the stratification within the region. We will first describe the model configuration in
131 detail and then compare against similarly-forced lower-resolution simulations to understand
132 how changes in horizontal resolution impacts model results in the Labrador Sea.

133

134 2. Methods

135 The numerical model used for our high-resolution simulation is the Nucleus for
136 European Modelling of the Ocean (NEMO; Madec, 2008), version 3.6, which is coupled to a sea-
137 ice model, LIM2 (Fichefet and Maqueda, 1997). The $1/4^\circ$ Arctic Northern Hemisphere Atlantic
138 configuration (ANHA4; Fig 1a) is used and includes a double nest via the Adaptive Grid
139 Refinement in FORTRAN package (AGRIF; Debreu et al., 2008). The AGRIF software allows for
140 high-resolution nests to communicate along their boundaries, passing information back and
141 forth between domains. The parent ANHA4 domain extends from Bering Strait, through the
142 Arctic and North Atlantic, to 20°S in the South Atlantic. The parent domain's nest uses a spatial
143 and temporal refinement factor of three, bringing resolution to $1/12^\circ$ and the time step to 240s
144 (Table 1) in the North Atlantic Sub Polar Gyre domain (SPG12; Fig 1b). An ANHA4 configuration
145 with a SPG12 nest has been evaluated before by investigating how model resolution influences

146 Labrador Sea Water formation (Garcia-Quintana et al., 2019) as well as eddy formation and
147 eddy fluxes in the North Atlantic Current (Müller et al., 2017; Müller et al., 2019). Another nest
148 is implemented within the SPG12 domain, using a spatial and temporal refinement of five,
149 increasing the horizontal resolution from $1/12^\circ$ to $1/60^\circ$ and reducing the time step to 48s
150 within the Labrador Sea (LAB60; Fig 1c). All nests allow two-way communication such that the
151 parent domain supplies boundary conditions while the daughter domain returns interpolated
152 values to all associated parent grid points. All domains have different horizontal grid spacing
153 but they share the same vertical grid which is set to 75 geopotential levels (Fig. 1d) using partial
154 steps (Barnier et al., 2006). This simulation involves three domains (ANHA4, SPG12, and LAB60)
155 although we primarily discuss what occurs within the $1/60^\circ$ nest.

156 A total variance dissipation scheme (Zalesak, 1979) was used in all domains to calculate
157 horizontal advection. A Laplacian operator was used to compute lateral diffusion in all domains,
158 while a bi-laplacian operator was used for lateral momentum mixing. As some model
159 parameters are grid-scale dependent, Table 1 displays these settings. As lateral boundary
160 conditions have been shown to be very important at producing Irminger Rings in high-
161 resolution simulations (Rieck et al. 2019), we used no-slip lateral boundary conditions within
162 the LAB60 domain while the other domains had free-slip conditions. Model mixed layer depths
163 were calculated via the vertical gradient in temperature and salinity (Holte and Talley, 2009) as
164 opposed to a 0.01 kg m^{-3} change in potential density between the surface and the bottom of
165 the mixed layer; the latter method can produce deeper mixed layers than observations suggest
166 (Courtois et al., 2017). Settings not listed in Table 1 indicate that all domains have an identical
167 value or option; some of these important settings are shown in Table 2.

168 Model bathymetry was interpolated from the $1/60^\circ$ ETOPO GEBCO dataset (Amante and
169 Eakins, 2009) to each domain's grid and bathymetric smoothing along nest boundaries was
170 carried out in order to conserve volume where the parent domain supplies boundary conditions
171 to the daughter domain. All domains were initialized from GLORYS1v1 (Ferry et al., 2009), a
172 global reanalysis ocean simulation, at the beginning of 2002. Monthly open boundary
173 conditions (3D T, S, U, V, and 2D SSH and ice values) across Bering Strait and 20° S were
174 supplied to the ANHA4 domain. These boundary conditions were linearly interpolated from

175 monthly values, overriding the values within the boundary without the use of a sponge layer.
176 Runoff was supplied via Dai et al. (2009) while we also included Greenland runoff as estimated
177 from a surface mass-balance model (Bamber et al., 2012). Without an iceberg model
178 functioning with the AGRIF software, we treated all solid runoff as a liquid, thus capturing the
179 full freshwater mass at the cost of accuracy in the spatial and temporal placement of
180 freshwater emitted from icebergs.

181 Precipitation, shortwave radiation, downward longwave radiation, 2 meter specific
182 humidity, 2 meter temperature, 10 meter meridional and 10 meter zonal winds originally were
183 supplied from the Canadian Meteorological Centre's Global Deterministic Prediction System's
184 Reforecast product (CGRF; Smith et al., 2014). While high in temporal (hourly) and spatial
185 resolution (33 km in the Labrador Sea), we found the air-sea fluxes were slightly too weak to
186 sustain deep convection after 2010. Rather than start completely over, we switched the
187 atmospheric forcing in 2007 (Fig. 2) when LAB60's mixed layer was still similar to observations.
188 Starting on 1 Jan 2007, we used the DRAKKAR Forcing Set 5.2 (DFS; Dussin et al., 2016). DFS
189 supplies data at 3 hour increments for wind, temperature, and humidity, while precipitation
190 and radiation are daily. DFS has a spatial resolution which is approximately 45 km within the
191 Labrador Sea. Our own analysis of the CGRF data showed a 2002-2015 average yearly heat loss
192 of 47 W m^{-2} from the interior Labrador Sea while DFS removed 53 W m^{-2} (Pennelly and Myers,
193 submitted). Increasing the horizontal resolution likely increased the horizontal buoyancy fluxes
194 and rendered the CGRF's air-sea heat loss, which was appropriate in our ANHA4 and ANHA12
195 configurations, inadequate. The decision to swap to DFS was based on its greater heat loss,
196 promoting a better mixed layer depth throughout the Labrador Sea, though a different forcing
197 product will eventually be needed as DFS does not currently extend past 2017. Supplemental
198 Fig. 1 depicts the difference in mixed layer depth between the LAB60 simulation forced by
199 CGRF, when forced with CGRF through 2007 and then forced by DFS, as well as what ARGO
200 observations suggest. The weaker air-sea heat loss as forced by the CGRF product leaves the
201 mixed layer with little interannual variability that doesn't compare well with observations.

202 Early testing showed that adding passive tracers increases the computing resources
203 required by about 20% per passive tracer. To keep the simulation from requiring too many
204 resources, we limited LAB60 to three passive tracers:

- 205 1. Liquid runoff from Greenland
- 206 2. Irminger Water ($T > 3.5^{\circ}\text{C}$, $S > 34.88$) which flows westward past Cape Farwell (Fig. 3b)
- 207 3. Labrador Sea Water ($\sigma_{\theta} > 27.68 \text{ kg m}^{-3}$) formed within the mixed layer of the Labrador
208 Sea (Fig. 3c)

209 Runoff from Greenland was included due to the importance of Greenland's freshwater
210 contribution to changes within the Labrador Sea. Water mass definitions for Irminger Water
211 and Labrador Sea Water were selected based on previous studies (i.e. Kieke et al., 2006; Myers
212 et al., 2007). Note that there is no maximum density criteria given to our Labrador Sea Water
213 tracer- the tracer is formed throughout the water column until it reaches the bottom of the
214 mixed layer. Figure 3 illustrates both the source regions as well as the tracer extent as of 1 Jan
215 2010. While these water masses have been studied before (Kieke et al., 2006; Myers et al.,
216 2007; Böning et al., 2016), there has been no attempt to use them as passive tracers at a
217 resolution higher than $1/20^{\circ}$ (Böning et al., 2016).

218 The LAB60 simulation originally started on the Graham cluster of Compute Canada.
219 Other high-resolution simulations often use thousands of computer processors but our
220 simulation could not run on more than 672 CPUs on this cluster as it would stall during domain
221 construction. The years 2002-2007 were carried out on Graham, after which a new allocation
222 on a different high performance Compute Canada cluster, Niagara, became available to us. The
223 LAB60 simulation on Niagara did not suffer from the same issue as it did on Graham and we
224 were able to use many more processors. Initial testing found a substantial increase in the
225 number of days simulated per job submission when the number of CPUs was increased from
226 672 to 3000; tests using 4000 CPUs showed no further improvement. Thus, we carried out the
227 remainder of the LAB60 simulation with 3000 CPUs. Each job submission required around 22
228 hours to carry out, providing 40 days of model output. The real time to finish each 40 day
229 submission naturally varied across the year, increasing during winter which we attribute to the
230 sea-ice model.

231 A spin-up period (Fig. 2) was required as the model quickly went unstable and crashed.
232 We attribute this to the interpolation of the $1/12^\circ$ GLORYS1v1 data onto the LAB60 grid; the
233 resulting data were not smooth enough and numerical noise was generated, leading to model
234 failure. To reduce this noise, a gradual spin-up procedure took place. First, we kept the
235 numerical timestep very low (2s in LAB60) when the model was initialized. We also set the
236 $1/60^\circ$ nests' eddy viscosity and diffusivity values to be equal to those within the SPG12 nest.
237 We gradually increased the timestep and reduced the viscosity and diffusivity values over the
238 first year (2002) to what is within Table 1. Other than also increasing the timestep to stay in line
239 with LAB60, no other values were changed across the coarser ANHA4 and SPG12 domains. To
240 allow LAB60 to adjust to the final settings, we consider the 2003 year to be an adjustment year
241 (Fig. 2).

242 To assess the validity of LAB60, model results were compared against AVISO satellite
243 data (<https://www.aviso.altimetry.fr/>), specifically U/V geostrophic velocities which are derived
244 from the sea surface height. Argo profiler data (<http://www.argo.net/>) was also used to assess
245 the mixed layer. Bottle data from cruise 18HUD20080520, accessed from CCHDO
246 (<https://cchdo.ucsd.edu/cruise/18HU20080520>) on 10 April 2018 was used to compare
247 observations across the AR7W section.

248

249 3. Model Simulation Results

250 To understand what is gained by resolving the Labrador Sea at $1/60^\circ$, we compare the
251 output of our LAB60 simulation with similarly forced ANHA simulations at both $1/4^\circ$ (ANHA4)
252 and $1/12^\circ$ (ANHA12). The large-scale circulation (top 50m) is shown for our 3 simulations (Fig. 4)
253 as well as AVISO geostrophic velocities. All simulations have greater speed within the West
254 Greenland Current (ANHA4: up to 0.8; ANHA12: 0.8; LAB60: 0.6; AVISO: 0.4 m s^{-1}) and Labrador
255 Current (ANHA4: up to 0.6; ANHA12: 0.6; LAB60: 0.4; AVISO: 0.4 m s^{-1}) as altimetry observations
256 suggest slower speeds here. However, Lin et al., (2018) found maximum speed up to 0.74 m s^{-1}
257 along the west coast of Greenland. Both the ANHA4 and ANHA12 configuration have larger
258 values further up the western coast of Greenland, as well as connecting the West Greenland
259 Current and the Labrador Current; features that do not occur in both LAB60 and observations.

260 As LAB60 and observations have less average speed occurring within these boundary currents,
 261 we suspect that all configurations have some large differences in eddy activity, particularly
 262 where these boundary currents are.

263 Eddy kinetic energy (EKE: $0.5(\overline{U_g'^2} + \overline{V_g'^2})$, Fig. 5) was calculated from geostrophic
 264 velocity anomaly based on the sea level anomaly (SLA) from the 2004-2013 mean state:

$$U_g' = -\frac{g SLA}{f \Delta y}$$

$$V_g' = -\frac{g SLA}{f \Delta x}$$

265 where g is the gravitational constant, f is the Coriolis parameter, and Δy and Δx are model grid
 266 length. Overbars indicate the 2004-2013 mean value while primed variables indicate a deviation
 267 from the mean state. AVISO observations were already supplied as geostrophic velocities.
 268 High levels of EKE can be found along the west coast of Greenland (Fig. 5), extending into the
 269 interior of the basin around 62° N, as well as along the Labrador coast's shelf break. The path
 270 extending from the west coast of Greenland is mostly due to Irminger Rings which leave this
 271 coast and travel westward (Chanut et al., 2008). While the EKE extending from west Greenland
 272 enters the interior of the Labrador Sea, that which stems from the Labrador coast does not
 273 penetrate far into the interior. The ANHA4 simulation has low EKE along the west coast of
 274 Greenland (around $100 \text{ cm}^2 \text{ s}^{-2}$) and along the Labrador Coast's shelf break ($10\text{-}30 \text{ cm}^2 \text{ s}^{-2}$). The
 275 ANHA12 simulation shows improvement, having much higher EKE extending from west
 276 Greenland ($100\text{-}300 \text{ cm}^2 \text{ s}^{-2}$) however the EKE does not quite extend into the interior of the
 277 Labrador Sea but instead remains in the northern Labrador Sea. Furthermore, there is
 278 additional EKE along the Labrador shelf break ($30\text{-}50 \text{ cm}^2 \text{ s}^{-2}$) compared against ANHA4. The
 279 LAB60 simulation shows further improvement as the EKE signature from the west Greenland
 280 coast is greater ($100\text{-}1000 \text{ cm}^2 \text{ s}^{-2}$) and now enters into the interior of the Labrador Sea. A
 281 notable increase in EKE also occurs along the Labrador shelf break ($100\text{-}200 \text{ cm}^2 \text{ s}^{-2}$) and within
 282 the interior Labrador Sea ($10\text{-}100 \text{ cm}^2 \text{ s}^{-2}$). LAB60 matches well against observations along the
 283 west coast of Greenland and the Labrador shelf break (both above $1000 \text{ cm}^2 \text{ s}^{-2}$) as well as the
 284 interior Labrador Sea ($10\text{-}100 \text{ cm}^2 \text{ s}^{-2}$). LAB60's higher interior EKE may be partially from
 285 convective eddies that are formed during the wintertime. However, LAB60 has lower EKE within

286 the Northwest Corner where ANHA4, ANHA12, and the observations exceed $1000 \text{ cm}^2 \text{ s}^{-2}$ over a
 287 wide area. LAB60 matches the spatial distribution albeit with reduced EKE.

288 The differences in the EKE field between these configurations identify that each
 289 simulation is resolving features of varying spatial scales. The ANHA4 simulation, with low EKE
 290 within the Labrador Sea, does not adequately resolve eddies in this region, as illustrated with a
 291 snapshot of normalized model relative vorticity (Fig. 6). However, the larger scale meanders
 292 within the North Atlantic Current are visible. ANHA12 shows a greater degree of mesoscale
 293 features (50 to 500 km), though distinct eddies within the Labrador Sea are also not resolved.
 294 LAB60 resolves eddies along both the west coast of Greenland as well as the Labrador Coast. A
 295 video showing LAB60's normalized relative vorticity is shown in Supplementary Video 1.

296 A few Irminger Rings are shown in Fig. 7, a snapshot in time from 26 July 2007. A newly
 297 spawned ring (Fig. 7c) shows very strong surface speeds (up 0.6 m s^{-1} for Ring A; Fig. 7a) while
 298 older eddies to the south have reduced speeds (up to 0.3 m s^{-1} for Ring B; Fig. 7a). To
 299 investigate the stratification strength, we calculate the amount of energy needed to produce a
 300 neutrally stratified column extending down to some reference depth, h . This proxy, called
 301 convective energy, is given by:

$$\text{Convective energy}(h) = \frac{g}{\text{Area}} \int \int \left[h \rho_{\theta}(h) - \int_0^h \rho_{\theta}(z) dz \right] dA$$

302 where g is the gravitational constant, Area is the total surface area over our region of interest
 303 (Fig. 1c), h is the reference depth (2000m used in this study), $\rho_{\theta}(z)$ and $\rho_{\theta}(h)$ are the potential
 304 density at each grid cell and the potential density of the grid cell at the reference depth, and A
 305 is the surface area of each grid cell. A strongly stratified column of water corresponds to a high
 306 convective energy value. A snapshot of convective energy (Fig. 7b) shows that most of these
 307 eddies have substantially higher amounts compared to the background Labrador Sea,
 308 suggesting that the cool and fresh WGC water, as well as warm and salty Irminger Water keep
 309 these eddies strongly stratified. However, these eddies age within the Labrador Sea, and while
 310 a new eddy has strong stratification ($>3000 \text{ J m}^{-3}$), an eddy which has evolved over many
 311 months (Fig. 7d) has weaker stratification (about 2000 J m^{-3}). Older eddies may have very weak
 312 stratification as they may have experienced two convective winter periods of buoyancy

313 removal. This has been noted before, as Lilly et al. (2003) found aged Irminger Rings with a
314 mixed layer that surpassed 1000m.

315 These differences in resolving the mesoscale (50 to 500 km) and sub-mesoscale (<50
316 km) processes within each simulation produced significant changes within the Labrador Sea as
317 seen from modeled convective energy values as averaged from 2004-2013 (Fig. 8). Resolving
318 few eddies, the ANHA4 simulation's interior Labrador Sea lacks the buoyancy flux and remains
319 very weakly stratified across a wide region. The ANHA12 simulation partially resolves some
320 mesoscale features and eddy fluxes from the Greenland coast which supplies buoyancy to the
321 Northern Labrador Sea and has higher convective energy. Furthermore, the spatial extent of
322 the weakly stratified region has shrunk and resides primarily within the Labrador Sea, as
323 opposed to ANHA4 which spills out of the basin. LAB60, fully capable of resolving buoyant
324 eddies from the Greenland and Labrador coast, as well as convective eddies, has a much
325 stronger degree of stratification in the interior region. A visible path of strong stratification
326 appears around 60°N along this coastline, eventually extending away from the coastline around
327 62°N. This path is consistent with the general path that simulated Irminger Rings take (Chanut
328 et al., 2008). Supplemental Video 2 shows the convective energy of the LAB60 simulation from
329 2004 through the end of 2013.

330 The ANHA4 simulation experiences weaker stratification in the Labrador Sea than
331 ANHA12 and LAB60, driving a deeper maximum mixed layer that also covers a larger spatial
332 extent (Fig. 9). However, the maximum mixed layer depth as simulated by ANHA4 and ANHA12
333 greatly exceed what Argo observations suggest (Fig. 9d). ANHA12 has higher EKE within the
334 WGC, supplying more buoyancy to the northern portion of the Labrador Sea, reducing both the
335 vertical extent of the mixed layer as well as the spatial extent where the mixed layer is deeper
336 than 1000m. LAB60 has higher EKE than ANHA12, and the vertical and spatial extent of deep
337 mixing is reduced even further. LAB60's mixed layer is far more similar to what ARGO
338 observations suggest, suggesting the additional eddy fluxes to be fairly accurate. The evolution
339 of LAB60's mixed layer depth is shown in supplemental video 3 from 2004 through the end of
340 2013.

341 After the bottom of the mixed layer returns to the near-surface, a newly formed LSW
342 mass is left behind. To account for density drift, we allow the LSW classification to evolve in
343 time, unlike our LSW passive tracer. We calculated LSW density and thickness by binning by
344 potential density, referenced to 1000 dbar, with bin lengths of 0.001 kg m^{-3} . This was carried
345 out within the black outlined polygon in Fig 1c for each daily output file per year. The density
346 bin which had the thickest layer across the year was set as the maximum density of LSW for
347 that year. The minimum density was defined to be 0.02 kg m^{-3} less than the maximum density.
348 Linear interpolation occurred between years to allow for a gradual shift in density to prevent
349 staircase patterns from emerging. Large differences in both the density as well as the thickness
350 are present between the simulations shown in Fig. 10. The ANHA4 and ANHA12 simulations
351 have similar density values of LSW while the LAB60 simulation is less dense. While the
352 interannual variability matches fairly well across all configurations, the density values suggested
353 by LAB60 are closer to ARGO observations (32.34 to 32.36 kg m^{-3} ; Yashayaev and Loder, 2016)
354 during the same time period. We suspect the denser LSW formed by ANHA4 and ANHA12 is
355 primarily attributed to the lack of buoyancy coming from Greenland. As similar air-sea heat
356 losses should occur in all three configurations, the weaker stratification of ANHA4 and ANHA12
357 indicates that deep mixing is more likely producing not only a denser LSW layer, but also a
358 thicker one. Yashayaev and Loder (2016) also investigated the thickness of LSW (their Fig. 8),
359 and while our simulations do not quite capture the same interannual variability and amplitude
360 suggested their analysis using ARGO profilers, LAB60 is far more accurate than the lower-
361 resolution configurations.

362 All simulations encounter some degree of numerical drift within the Labrador Sea (Fig.
363 11), judging from the salt and heat content change as calculated between the surface and
364 seafloor within the polygon in Figure 1 since 2004. ANHA4 experiences the largest drift in both
365 salt and heat, helping us understand why LSW is so dense in this simulation. ANHA12 also
366 experiences drift, though slightly less severe. LAB60 has a small but gradual increase in both salt
367 and heat content although it is difficult to state if this is drift or simply interannual to decadal
368 variability. Regardless of the cause, LAB60's change in both heat and salt content is very
369 minimal compared against the lower-resolution simulations.

370 When compared against bottle data collected during a single hydrographic cruise across
371 Atlantic Repeat Hydrography Line 7 West (AR7W; Fig 12), LAB60 is slightly warmer (about 0.25
372 °C) and saltier (about 0.05 kg m^{-3}) throughout the interior. This causes LAB60 to be slightly
373 denser with isopycnals residing higher than observations during this cruise suggest.
374 Observations were not carried out above Greenland's continental slope, although they show
375 some presence of the warm core of the WGC which the model captures. Salinity values close to
376 the Labrador coast compare well while LAB60 is slightly warmer (about $0.5 \text{ }^\circ\text{C}$) above the
377 continental shelf.

378 The three passive tracers implemented within the full LAB60 configuration (Fig. 3) show
379 where Greenland runoff, Irminger Water, and Labrador Sea Water travel to. These tracers were
380 selected because they either contain a significant amount of buoyant water compared to the
381 Labrador Sea, or are produced via convection in the Labrador Sea. From this image on 1 Jan
382 2010, we see a large portion of Greenland's runoff (Fig. 3a) resides within Baffin Bay as well as
383 along the Labrador Coast. Some of this tracer is present where the ocean depth is greater than
384 2000m. A few Irminger Rings are identifiable, due to their thicker freshwater cap, which are in
385 water deeper than 3000m. Little exchange with the interior basin appears to occur along the
386 Labrador Current until the vicinity of Flemish Cap, after which a significant portion of the tracer
387 propagates eastward. Supplemental Video 4 shows this the evolution of this tracer from 2004
388 through the end of 2013.

389 Irminger Water ($T > 3.5^\circ\text{C}$, $S > 34.88$; Fig. 3b) which flows west past Cape Farwell, enters
390 the interior Labrador Sea with the greatest amounts where the seafloor is at a depth between
391 2000 and 3000m. Similar as above, individual Irminger Rings are visible, containing a larger
392 amount of Irminger Water than the surrounding water. This water mass also flows along the
393 Labrador Coast until it is in the vicinity of Flemish Cap. Supplemental Video 5 shows this the
394 evolution of this tracer from 2004 through the end of 2013.

395 Our Labrador Sea Water tracer (Fig. 3c) is traced where the mixed layer produces water
396 with a potential density above $1027.68 \text{ kg m}^{-3}$ within the black contour identified in the figure.
397 This definition differs compared to our method of classifying LSW as we did not implement any
398 FORTRAN code to detect and compensate for density drift of our simulation, instead sticking to

399 a strict density classification for this tracer. As this image was made at the start of the
400 convection season, the current deep patch is a freshly produced layer that reaches up to 800m
401 deep. After forming, LSW spreads southwards along the Labrador shelf break as well as to the
402 southeast. Supplemental Video 6 shows this the evolution of this tracer from 2004 through the
403 end of 2013.

404 4. Discussion

405 We describe a 10+ year long, high-resolution simulation which achieves $1/60^\circ$ horizontal
406 resolution in the Labrador Sea via two nests inside a regional configuration, resolving mesoscale
407 and sub-mesoscale processes which strongly impact the deep convection which occurs here.
408 We show that lower-resolution simulations fail to resolve these key processes that strongly
409 control the production of Labrador Sea Water, an important water mass within the Atlantic
410 Meridional Overturning Circulation. While the NATL60 and eNATL60 simulations were designed
411 with the SWOT altimetry satellite mission in mind (NATL60 website: [https://meom-](https://meom-group.github.io/swot-natl60/virtual-ocean.html)
412 [group.github.io/swot-natl60/virtual-ocean.html](https://meom-group.github.io/swot-natl60/virtual-ocean.html)), their integration period, like many other high-
413 resolution simulations, is a handful of years. LAB60, although covering a much smaller region,
414 could be a valuable asset to many users who require a lengthy period of high-resolution model
415 output. We also have included three passive tracers which are often excluded in simulations at
416 this resolution. Our three passive tracers highlight regions where each water mass enters the
417 interior region of the Labrador Sea, demonstrating the pathways of buoyant Greenland melt
418 and Irminger water. Furthermore, we trace Labrador Sea Water which is formed during the
419 convective winter period.

420 We show that LAB60 has greater EKE than our lower-resolution simulation, resolving
421 eddy fluxes including Irminger Rings, boundary current eddies, and likely convective eddies as
422 indicated by greater EKE within the interior. Boundary current eddies still appear relatively
423 disconnected from the interior basin, adding further support that these eddies have limited
424 influence on convection and restratification (Rieck et al., 2019). We offer no additional support
425 regarding the relative importance of Irminger Rings and convective eddies on controlling deep
426 convection; this is currently being investigated for a later manuscript. Model drift appears very
427 low, a large improvement over the ANHA4 and ANHA12 configurations. The drift might produce

428 slightly denser LSW than observations suggest, however LAB60s density is much more accurate
429 than ANHA4 and ANHA12. The boundaries of LAB60, supplied by the inner SPG12 nest, may
430 influence the high-resolution nest. We note that the North Atlantic Current, which is close to
431 the boundary, has less EKE and vorticity than the ANHA4 and ANHA12 simulations. Conversely,
432 the WGC close to the eastern nested boundary has multiple jets which have been noted in
433 hydrographic data (Pickart, personal communication). Boundary communication is always a
434 concern in nested simulations and LAB60 is no different. More investigation will reveal any
435 potential boundary issues but our results so far indicate no further areas of potential concern.

436 Others have investigated the Labrador Sea using numerical simulations with different
437 resolution. Böning et al. (2016) traced Greenland meltwater with the $1/20^\circ$ VIKING20 and $1/4^\circ$
438 ORCA025 simulations, noting more meltwater entered the interior Labrador Sea at higher
439 resolution partially as a result of greater WGC eddy fluxes but not from the Labrador coast. The
440 minor amount of eddy fluxes from the Labrador coast has been noted earlier even at lower
441 resolution ($1/3^\circ$; Myers, 2005). Steadily increasing horizontal resolution has so far not changed
442 this for the Labrador coast, though this is opposite for the WGC. LAB60 has a clear increase in
443 EKE and likely greater eddy fluxes from the WGC into the interior of the Labrador Sea.

444 We have many ambitious research topics which we plan to use LAB60 to investigate.
445 This includes, but is not limited to, the variability and structure of the West Greenland Coastal
446 Current, Labrador Sea Water production, and the role of both Irminger Rings and convective
447 eddies in controlling stratification in the Labrador Sea. This lengthy high-resolution simulation
448 with three passive tracers will provide valuable information for many numerical studies within
449 the Labrador Sea for years to come.

450

451 Code and/or data availability

452 The FORTRAN code used to carry out the LAB60 simulation can be accessed from the
453 NEMO version 3.6 repository
454 (<https://forge.ipsl.jussieu.fr/nemo/browser/NEMO/releases/release-3.6>). A few FORTRAN files
455 were modified to handle our passive tracers. The complete FORTRAN files as well as the
456 CPP.keys, namelists, and associated files can be found on Zenodo (Pennelly, 2020). Initial and

457 boundary conditions, atmospheric forcing, and numerical output were too large to host on a
458 repository and instead are hosted on our lab's servers as well as the Compute Canada Niagara
459 server. These data can be requested by emailing the corresponding author.

460

461 Author Contribution

462 PM designed the layout of the LAB60 configuration which included the region of
463 interest, numerical length, and which forcing and initial conditions to supply, as well as
464 supervised CP. CP produced the configuration, modified the FORTRAN code, set up the
465 configuration on the high-performance computing systems, carried out the simulation, and
466 performed the analysis. The manuscript was prepared by CP with contributions by PM.

467

468 Acknowledgements

469 The authors would like to thank the NEMO development team as well as the DRAKKAR
470 group for providing the model code and continuous guidance. We express our thanks to
471 Westgrid and Compute Canada (<http://www.computecanada.ca>) for the computational
472 resources to carry out our numerical simulations as well as archival of the experiments. We
473 would like to thank Nathan Grivault for his help to migrate our configuration between
474 computing clusters, as well as Charlene Feucher for her help with ARGO data. This work was
475 supported by an NSERC Climate Change and Atmospheric Research Grant (Grant RGPCC
476 433898) as well as an NSERC Discovery Grant (Grant RGPIN 04357).

477

478 The authors declare that they have no conflict of interest.

479

480

481 References

482 Amante, C. and Eakins, B.W.: ETOPO1 1 Arc-minute global relief model: procedures data
483 sources and analysis. NOAA Technical Memorandum NESDIS, NGDC-24 19, 2009.

484 Bacon, S., Gould, W.J., and Jia, Y.: Open-ocean convection in the Irminger Sea. *Geophysical*
485 *Research Letters*, 30(5), 2003.

486 Bamber, J., van den Broeke, M., Ettema, J., Lenaerts, J., and Rignot, E.: Recent large increases in
487 freshwater fluxes from Greenland into the North Atlantic. *Geophysical Research Letters*, 39(19),
488 2012.

489 Barnier, B., Madec, G., Penduff, T., Molines, J.-M., Treguier, A.-M., Le Sommer, J., Beckmann, A.,
490 Biastoch, A., Böning, C., Dengg, J., Derval, C., Durand, E., Gulev, S., Remy, R., Talandier, C.,
491 Theetten, S., Maltrud, M., Mcclean, J., and De Cuevas, B.: Impact of partial steps and
492 momentum advection schemes in a global ocean circulation model at eddy permitting
493 resolution. *Ocean Dynamics*, 56 (5-6), 543-567, 2006.

494 Böning, C.W., Behrens, E., Biastoch, A., Getzlaff, K., and Bamber, J.L.: Emerging impact of
495 Greenland meltwater on deepwater formation in the North Atlantic Ocean. *Nature Geoscience*,
496 97(7), 523, 2016.

497 Brossier, C.L., Léger, L., Giordani, H., Beuvier, J., Bouin, M.N., Ducrocq, W., and Fourrié, N.:
498 Dense water formation in the north-western Mediterranean area during HyMeX-SOP2 in 1/36°
499 ocean simulations: Ocean-atmosphere coupling impact. *Journal of Geophysical Research:*
500 *Oceans*, 122(7), 5749-5773, 2017.

501 Bryden, H.L., Longworth, H.R., and Cunningham, S.A.: Slowing of the Atlantic meridional
502 overturning circulation at 25°N. *Nature*, 438(7068), 655, 2005.

503 Cael, B.B. and Jansen, M.F.: On freshwater fluxes and the Atlantic meridional overturning
504 circulation. *Limnology and Oceanography*, 5(2), 185-192, 2020.

505 Chanut, J., Barnier, B., Large, W., Debreu, L., Penduff, T., Molines, J.M., and Mathiot, P.:
506 Mesoscale eddies in the Labrador Sea and their contribution to convection and restratification.
507 *Journal of Physical Oceanography*, 28(8), 1617-1643, 2008.

508 Chassignet, E.P. and Xu, X.: Impact of horizontal resolution (1/12 to 1/50) on Gulf Stream
509 separation, penetration, and variability. *Journal of Physical Oceanography*, 47(8), 1999-2021,
510 2017.

511 Courtois, P., Hu, X., Pennelly, C., Spence, P., and Myers, P.G.: Mixed layer depth calculation in
512 deep convection regions in ocean numerical models. *Ocean Modelling*, 120, 60-78, 2017.

513 Cuny, J., Rhines, P.B., and Kwok, R.: Davis Strait volume, freshwater and heat fluxes. *Deep Sea*
514 *Research Part I: Oceanographic Research Papers*, 52.3, 519-542, 2005.

515 Curry, B., Lee, C.M., and Petrie, B.: Volume, freshwater, and heat fluxes through Davis Strait,
516 2004-05. *Journal of Physical Oceanography*, 41(3), 429-436, 2011.

517 Curry, B., Lee, C.M., Petrie, B., Moritz, R.E. and Kwok, R.: Multiyear volume, liquid freshwater,
518 and sea ice transports through Davis Strait, 2004-10. *Journal of Physical Oceanography*, 44(4),
519 1244-1266, 2014.

520 Dai, A., Qian, T., Trenberth, K.E., and Milliman, J.D.: Changes in continental freshwater
521 discharge from 1948 to 2004. *Journal of Climate*, 22(10), 2773-2792, 2009.

522 Debreu, L., Vouland, C., and Blayo, E.: AGRIF: Adaptive grid refinement in Fortran. *Computers*
523 *and Geosciences*, 34(1), 8-13, 2008.

524 Dussin, R., Barnier, B., and Brodeau, L.: The making of Drakkar forcing set DFS5, Grenoble,
525 France: LGGE, 2016.

526 Ferry, N., Parent, L., Garric, G., Barnier, B., and Jourdain, N.C.: Mercator global eddy permitting
527 ocean reanalysis GLORYS1V1: Description and results. *Mercator-Ocean Quarterly Newsletter*,
528 36, 15-27, 2010.

529 Fichfet, T., and Maqueda, M.A.M.: Sensitivity of a global sea ice model to the treatment of ice
530 thermodynamics and dynamics. *Journal of Geophysical Research: Oceans*, 102(C6), 12609-
531 12646, 1997.

532 Fischer, J., Visbek, M., Zantopp, R., Nunes, N.: Interannual to decadal variability of outflow from
533 the Labrador Sea. *Geophysical Research Letters*, 37(24), 2010.

534 Frajka-Williams, E., Rhines, P.B., and Eriksen, C.C.: Horizontal stratification during deep
535 convection in the Labrador Sea. *Journal of Physical Oceanography*, 44(1), 220-228, 2014.

536 Fratantoni, P.S. and Pickart, R.S.: The Western North Atlantic Shelfbreak Current System in
537 Summer. *Journal of Physical Oceanography*, 37(10), 2509-2533, 2007.

538 Fresnay, S., Ponte, A.L., Le Gentil, S., Le Sommer, J.: Reconstruction of the 3-D dynamics from
539 surface variable in a high-resolution simulation of the North Atlantic. *Journal of Geophysical*
540 *Research: Oceans*, 123(3), 1612-1630, 2018.

541 Garcia-Quintana, Y., Courtois, P., Hu, X., Pennelly, C., Kieke, D., and Myers, P.G.: Sensitivity of
542 Labrador Sea Water formation to changes in model resolution, atmospheric forcing, and
543 freshwater input. *Journal of Geophysical Research: Oceans*, 124(3), 2126-2152, 2019.

544 Gelderloos, R., Katsman, C.A. and Drijfhout, S.S.: Assessing the roles of three eddy types in
545 restratifying the Labrador Sea after deep convection. *Journal of Physical Oceanography*, 41(11),
546 2102-2119, 2011.

547 Gordon, A.L., Visbeck, M., and Comiso, J.C.: A possible link between the Weddell Polynya and
548 the Southern Annular Mode. *Journal of Climate*, 20(11), 2558-2571, 2007.

549 Hansen, B., and Østerhus, S.: North Atlantic-Nordic Seas exchanges. *Progress in Oceanography*,
550 45(2), 109-208, 2000.

551 Hátún, H., Eriksen, C.C., and Rhines, P.B.: Buoyant eddies entering the Labrador Sea observed
552 with gliders and altimetry. *Journal of Physical Oceanography*, 37(12), 2838-2854, 2007.

553 Holte, J., and Talley, L.: A new algorithm for finding mixed layer depths with applications to
554 Argo data and Subantarctic Mode Water formation. *Journal of Atmospheric and Oceanic*
555 *Technology*, 26(9), 1920-1939, 2009.

556 Kieke, D., Klein, B., Stramma, L., Rhein, M., and Koltermann, K.P.: Variability and propagation of
557 Labrador Sea Water in the southern subpolar North Atlantic. *Deep Sea Research Part I:*
558 *Oceanographic Research Papers*, 56(10), 1656-1674, 2009.

559 Lab Sea Group: The Labrador Sea deep convection experiment. *Bulletin of the American*
560 *Meteorological Society*, 79(10), 2033-2058, 1998.

561 Large, W.G., and Yeager, S.G.: The global climatology of an interannually varying air-sea flux
562 data set. *Climate Dynamics*, 33(2-3), 341-364, 2008

563 Latif, M., Roechner, E., Mikolajewicz, U., and Voss, R.: Tropical stabilization of the thermohaline
564 circulation in a greenhouse warming simulation. *Journal of Climate*, 13(11), 1809-1813, 2000.

565 Lazier, J., Hendry, R., Clarke, A., Yashayaev, I., and Rhines, P.: Convection and restratification in
566 the Labrador Sea, 1990-2000. *Deep Sea Research Part I: Oceanographic Research Papers*,
567 49(10), 1819-1835, 2002.

568 Lazier, J.R.N., and Wright, D.G.: Annual velocity variations in the Labrador Current, *Journal of*
569 *Physical Oceanography*, 23(4), 659-678, 1993.

570 Lilly, J.M., Rhines, P.B., Visbeck, M., Davis, R., Lazier, J.R.N., Schott, F., and Farmer, D.: Observing
571 deep convection in the Labrador Sea during winter 1994/95. *Journal of Physical Oceanography*,
572 29, 2065-2098, 1999.

573 Lilly, J.M., Rhines, P.B., Schott, F., Lavender, K., Lazier, J., Send, U., and D'Asaro, E.:
574 Observations of the Labrador Sea eddy field. *Progress in Oceanography*, 59(1), 75-176, 2003.

575 Lin, P., Pickart, R.S., Torres, D.J., and Pacini, A.: Evolution of the freshwater coastal current at
576 the southern tip of Greenland. *Journal of Physical Oceanography*, 48(9), 2127-2140. 2018

577 Madec, G.: Note du Pôle de modélisation. Institut Pierre-Simon Laplace (IPSL), France, No 27,
578 ISSN No 1288-1619, 2008.

579 Marshall, J. and Schott, F.: Open-ocean convection: Observations, theory, and models. *Reviews*
580 *of Geophysics*, 37(1), 1-64, 1999.

581 Marzocchi, A., Hurshi, J.J.M., Holiday, N.P., Cunningham, S.A., Blaker, A.T., and Coward, A.C.:
582 The North Atlantic subpolar circulation in an eddy-resolving global ocean model. *Journal of*
583 *Marine Systems*, 142, 126-143, 2015.

584 McGeehan, I. and Maslowski, W.: Impact of shelf-basin freshwater transport on deep
585 convection in the western Labrador Sea. *Journal of Physical Oceanography*, 41(11), 2187-2210,
586 2011.

587 Müller, V., Kieke, D., Myers, P.G., Pennelly, C., and Mertens, C.: Temperature flux carried by
588 individual eddies across 47° in the Atlantic Ocean. *Journal of Geophysical Research: Oceans*,
589 122(3), 2441-2464, 2017.

590 Müller, V., Kieke, D., Myers, P.G., Pennelly, C., Steinfeldt, R., and Stendardo, I.: Heat and
591 freshwater transport by mesoscale eddies in the southern subpolar North Atlantic. *Journal of*
592 *Geophysical Research: Oceans*, 124(8), 5565-5585, 2019.

593 Myers, P.: Impact of freshwater from the Canadian Arctic Archipelago on Labrador Sea water
594 formation. *Geophysical Research Letters*, 32(6), 2005.

595 Pennelly, C.: A 1/60 degree NEMO configuration within the Labrador Sea: LAB60, Zenodo,
596 <http://doi.org/10.5281/zenodo.3762748>, 2020.

597 Pennelly, C. Hu, X., and Myers, P.G.: Cross-isobath freshwater exchange within the North
598 Atlantic Subpolar Gyre. *Journal of Geophysical Research: Oceans*, 124(10), 6831-6853, 2019.

599 Rattan, S., Myers, P.G., Treguier, A.M., Theetten, S., Biastoch, A., and Böning, C. Towards an
600 understanding of Labrador Sea salinity drift in eddy-permitting simulations. *Ocean Modelling*,
601 35(102), 77-88, 2010.

602 Rieck, J.K., Böning, C.W., and Getzlaff, K.: The nature of eddy kinetic energy in the Labrador Sea:
603 Different types of mesoscale eddies, their temporal variability, and impact on deep convection.
604 *Journal of Physical Oceanography*, 49(8), 2075-2094, 2019.

605 Schmidt, S. and Send, U.: Origin and composition of seasonal Labrador Sea freshwater. *Journal*
606 *of Physical Oceanography*, 37(6), 1445-1454, 2007.

607 Schulze, L.M., Pickart, R.S., and Moore, G.W.K.: Atmospheric forcing during active convection in
608 the Labrador Sea and its impact on mixed-layer-depths. *Journal of Geophysical Research:*
609 *Oceans*, 121(9), 6978-6992, 2016.

610 Smith, G.C., Roy, F., Mann, P., Dupont, F., Brasnett, B., Lemieux, J.F., Laroche, S., and Bélair, S.:
611 A new atmospheric dataset for forcing ice-ocean models: Evaluation of reforecasts using the
612 Canadian global deterministic prediction system. *Quarterly Journal of the Royal Meteorological*
613 *Society*, 140(680), 881-894, 2014.

614 Straneo, F.: Heat and freshwater transport through the central Labrador Sea. *Journal of Physical*
615 *Oceanography*, 36(4), 606-628, 2006.

616 Straneo, F. and Saucier, F.: The arctic-subarctic exchange through Hudson Strait. *Arctic-*
617 *Subarctic Ocean Fluxes*, Springer, Dordrecht, 249-261, 2008.

618 De Steur, L., Hansen, E., Gerdes, R., Karcher, M., Fahrbach, E., Holfort, J.: Freshwater fluxes in
619 the East Greenland Current: A decade of observations. *Geophysical Research Letters*, 36(23),
620 2009.

621 Su, Z., Wang, J., Klein, P., Thompson, A.F., and Menemenlis, D.: Ocean submesoscales as a key
622 component of the global heat budget. *Nature communications*, 9(1), 1-8, 2018.

623 Tréquier, A.M., Theetten, S., Chassignet, E.P., Penduff, T., Smith, R., Talley, L., Beismann, J.O.,
624 and Böning, C.: The North Atlantic subpolar gyre in four high-resolution models. *Journal of*
625 *Physical Oceanography*, 35(5), 757-774, 2005.

626 Yashayaev, I. and Loder, J.W.: Recurrent replenishment of Labrador Sea Water and associated
627 decadal-scale variability. *Journal of Geophysical Research: Oceans*, 121(11), 8095-8814, 2016.

628 Yashayaev, I.: Hydrographic changes in the Labrador Sea, 1960-2005. *Progress in*
629 *Oceanography*, 73(3-4), 242-276, 2007.

630 Whitworth, T. and Orsi, A.H.: Antarctic Bottom Water production and export by tides in the
631 Ross Sea. Geophysical Research Letters 33(12), 2006.

632 Zalesak, S.T.: Fully multidimensional flux-corrected transport algorithms for fluids. Journal of
633 computational physics, 31(3), 335-362, 1979.

634

635 Tables

636

637 Table 1: Domain settings for the ANHA4 parent domain, SPG12 and LAB60 nested domains.

638 Other settings which are invariant to the domain are shown in Table 2.

| Setting | ANHA4 | SPG12 | LAB60 |
|--|----------------------|----------------------|-------------------|
| Horz. Resolution | 1/4° | 1/12° | 1/60° |
| X points | 544 | 724 | 1179 |
| Y points | 800 | 694 | 2659 |
| Timestep [s] | 720 | 240 | 48 |
| Horiz. Eddy Viscosity [$\text{m}^4 \text{s}^{-1}$] | 1.5×10^{11} | 1.5×10^{10} | 3.5×10^8 |
| Horiz. Eddy Diffusivity [$\text{m}^2 \text{s}^{-1}$] | 300 | 50 | 20 |
| Lateral Slip Conditions | Free slip | Free slip | No slip |

639

640

641

642

643

644

645

646

647

648

649

650

651

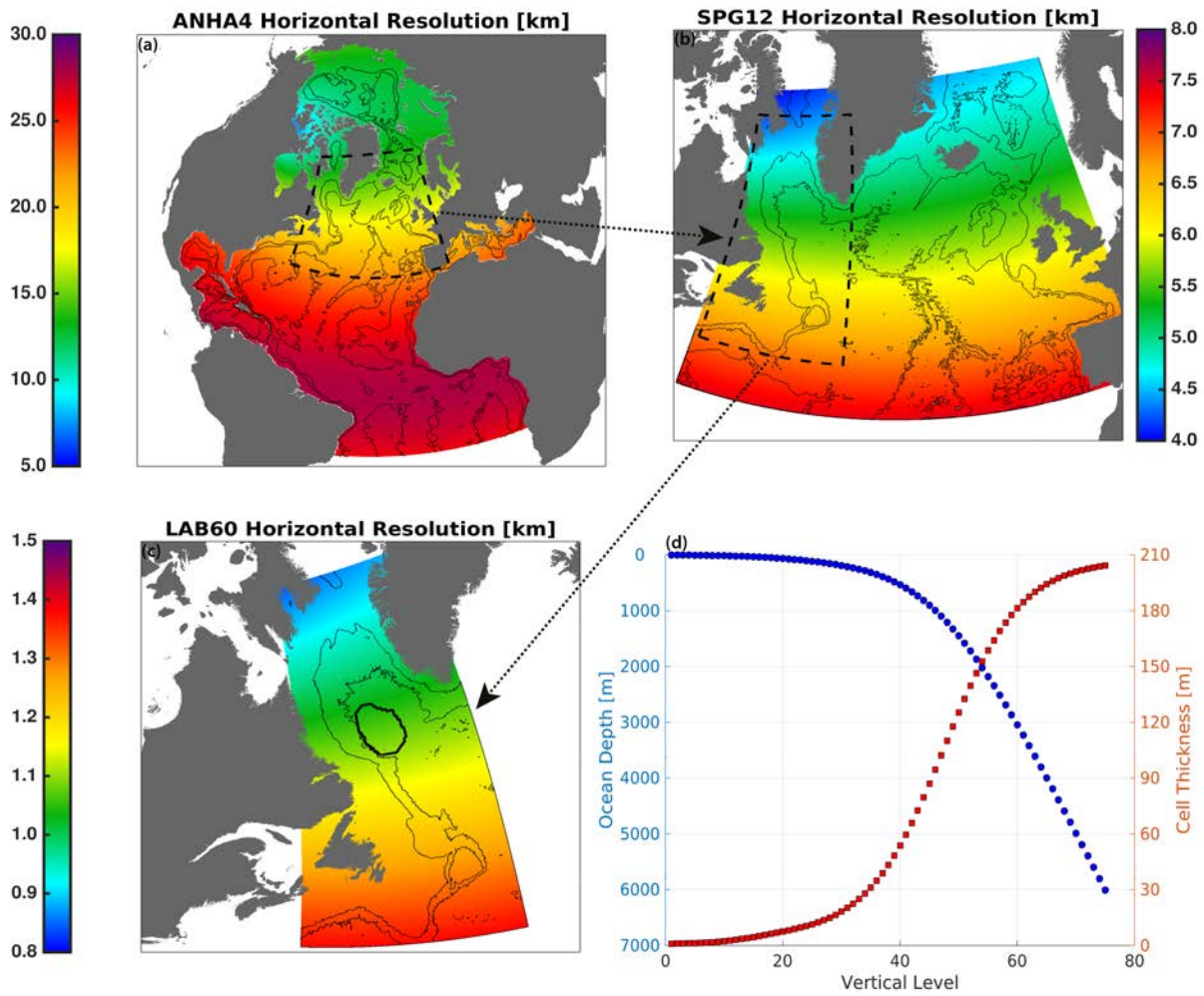
652 Table 2: Model configuration settings which are identical between all three domains. **Bold**
 653 values indicate values which were changed when we migrated LAB60 from the Graham cluster
 654 to Niagara.

| Configuration Setting | Value |
|---------------------------|--|
| Vertical grid | 75 geopotential levels |
| Sea-ice model | LIM 2 (Fichefet and Maqueda, 1997) |
| Bulk formula | CORE (Large and Yeager, 2008) |
| Liquid discharge | Dia et al. (2009) + Bamber (2012: Greenland) |
| Solid discharge | Input as liquid |
| Surface Restoring | None |
| Initial conditions | Glorys1v1 (T,S,U,V,SSH,ice) |
| Open boundary conditions | Glorys1v1 (T,S,U,V,ice) |
| Atmospheric forcing: | |
| | 2002-2006 CGRF (Smith et al, 2014) |
| | 2007-2017 Drakkar Forcing Set 5.2 (Dussin et al. 2016) |
| Lateral momentum | Bilaplacian operator |
| Lateral diffusion | Laplacian operator |
| Vertical eddy viscosity | $1 \times 10^{-4} \text{ m}^2 \text{ s}^{-1}$ |
| Vertical eddy diffusivity | $1 \times 10^{-5} \text{ m}^2 \text{ s}^{-1}$ |
| Mixed layer scheme | Holte and Talley (2009) |
| Bottom friction | Nonlinear |
| Hydrostatic approximation | Yes |
| Passive tracers | Three (see Figure 2) |
| CPU requested | 672 (3000), Broadwell 2.1 GHz (Skylake 2.4 GHz) |
| Time to complete 1 year | Approximately 700 (200) hours |
| Initialization date | January 1st, 2002 |

655

656

657 Figures

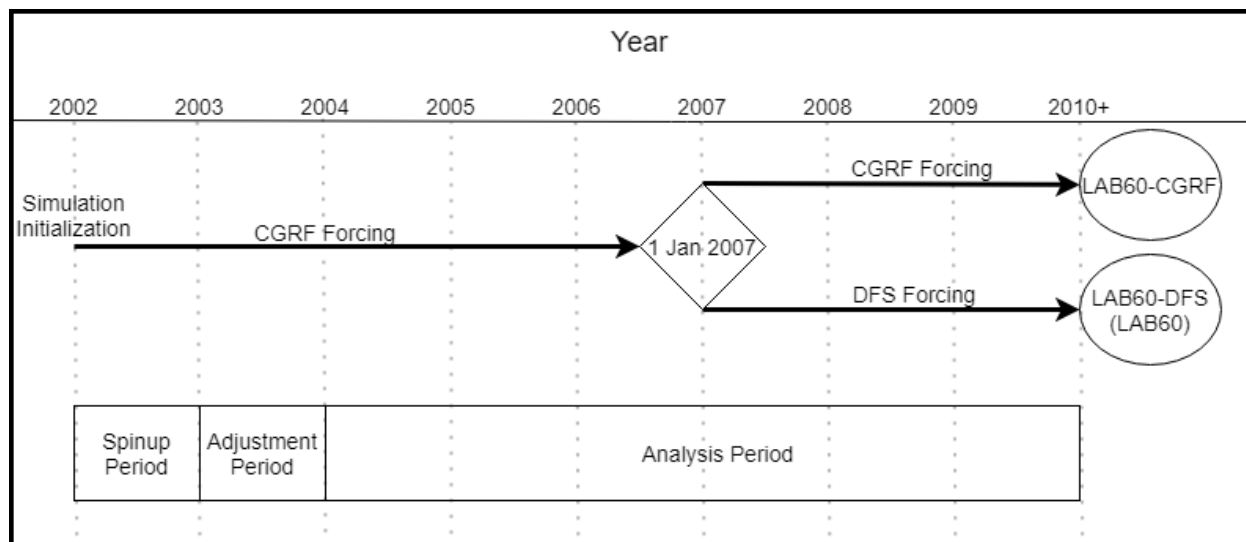


658

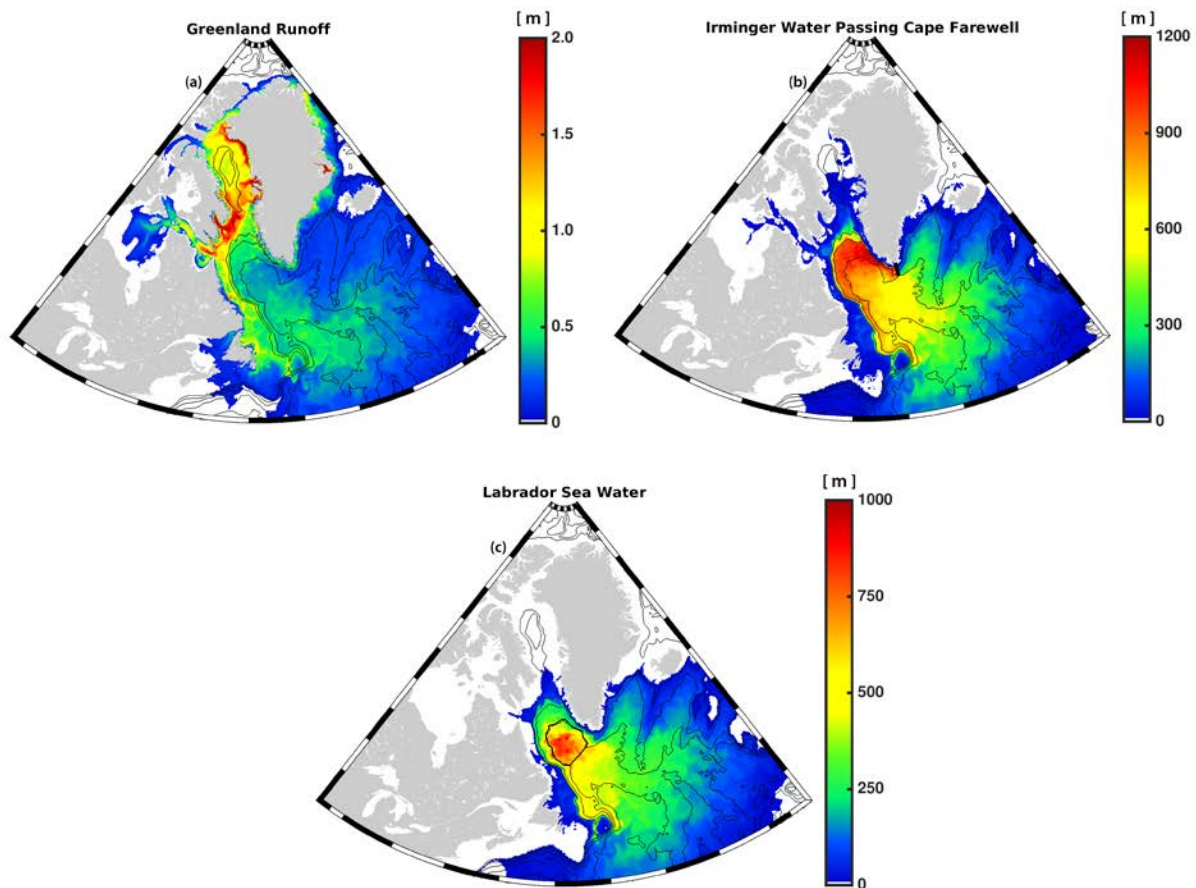
659 Figure 1: Domain setup for the (a) ANHA4 parent domain, (b) the SPG12 nest, and (c) the LAB60
 660 nest. Horizontal grid resolution, in km, is identified by color. All domains share identical vertical
 661 grid structure (d). The thick black contour in (c) identifies a region of interest where calculations
 662 of LSW's density, thickness, and mixed layer depth are determined. The 1000m, 3000m, and
 663 5000m isobaths are shown via the thin black contours.

664

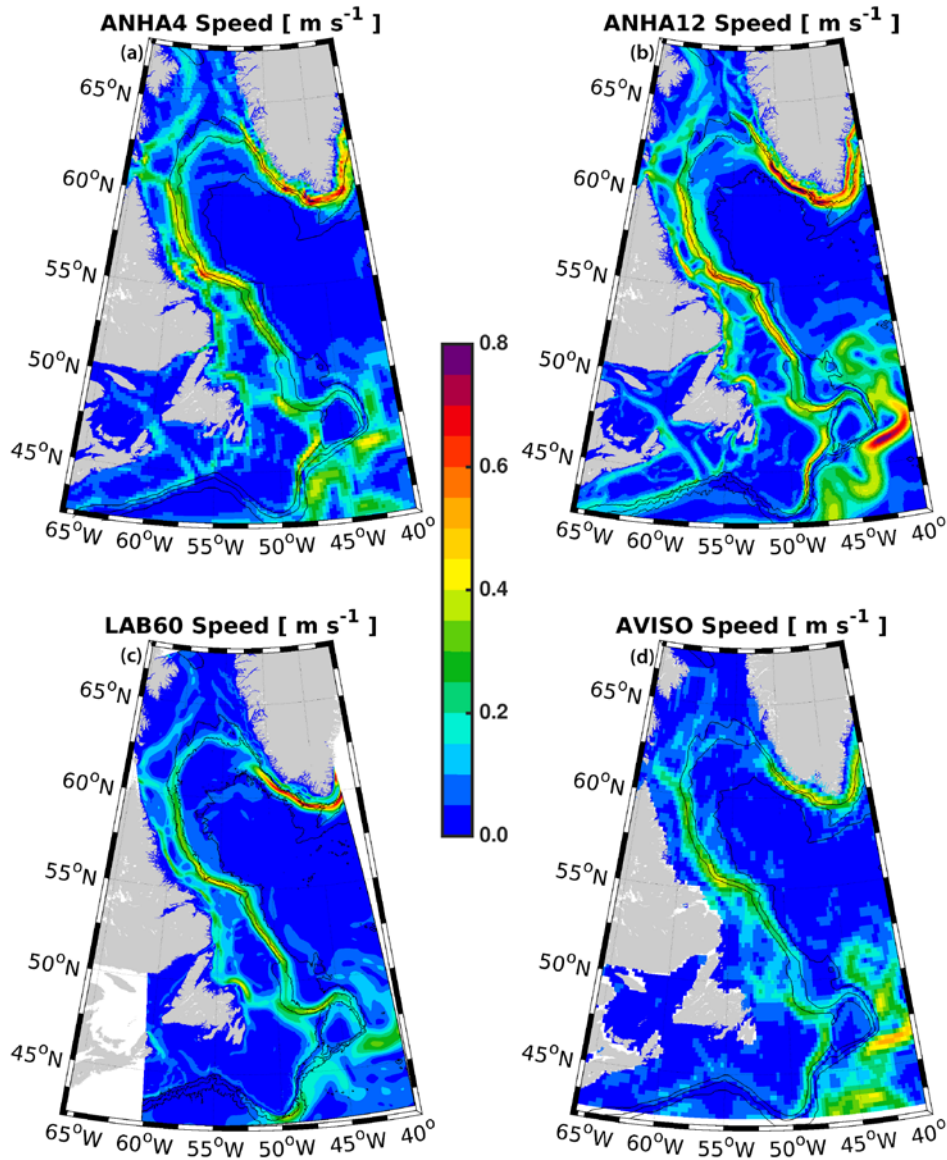
665



666
 667 Figure 2: Diagram showing the multiple periods of the LAB60 simulation. The original simulation
 668 was initialized with CGRF atmospheric forcing in 2002, although a branch swapping to DFS
 669 occurred at the start of 2007. This DFS branch is what is primarily presented in this study.
 670



671
 672 Figure 3: The three passive tracers used within our LAB60 simulation with source regions
 673 indicated by thick black lines: (a) Greenland runoff, (b) Irminger Water ($T > 3.5^{\circ}\text{C}$, $S > 34.88$)
 674 which flows west past Cape Farwell, and (c) Labrador Sea Water ($\sigma_{\theta} > 27.68 \text{ kg m}^{-3}$) produced
 675 each convective season. Images are from the simulation date 1 Jan 2010. Bathymetric contours
 676 are every 1000m. Units are the thickness, in meters, of the tracer. Note: as all three domains
 677 are included in this figure, spatial resolution changes within each subfigure.



678

679 Figure 4: Top 50m average speed (2004-2013) for the (a) ANHA4, (b) ANHA12, (c) and LAB60
 680 simulations, as well as (d) from AVISO observations. The 1000, 2000, and 3000m isobaths are
 681 shown by the black contour lines.

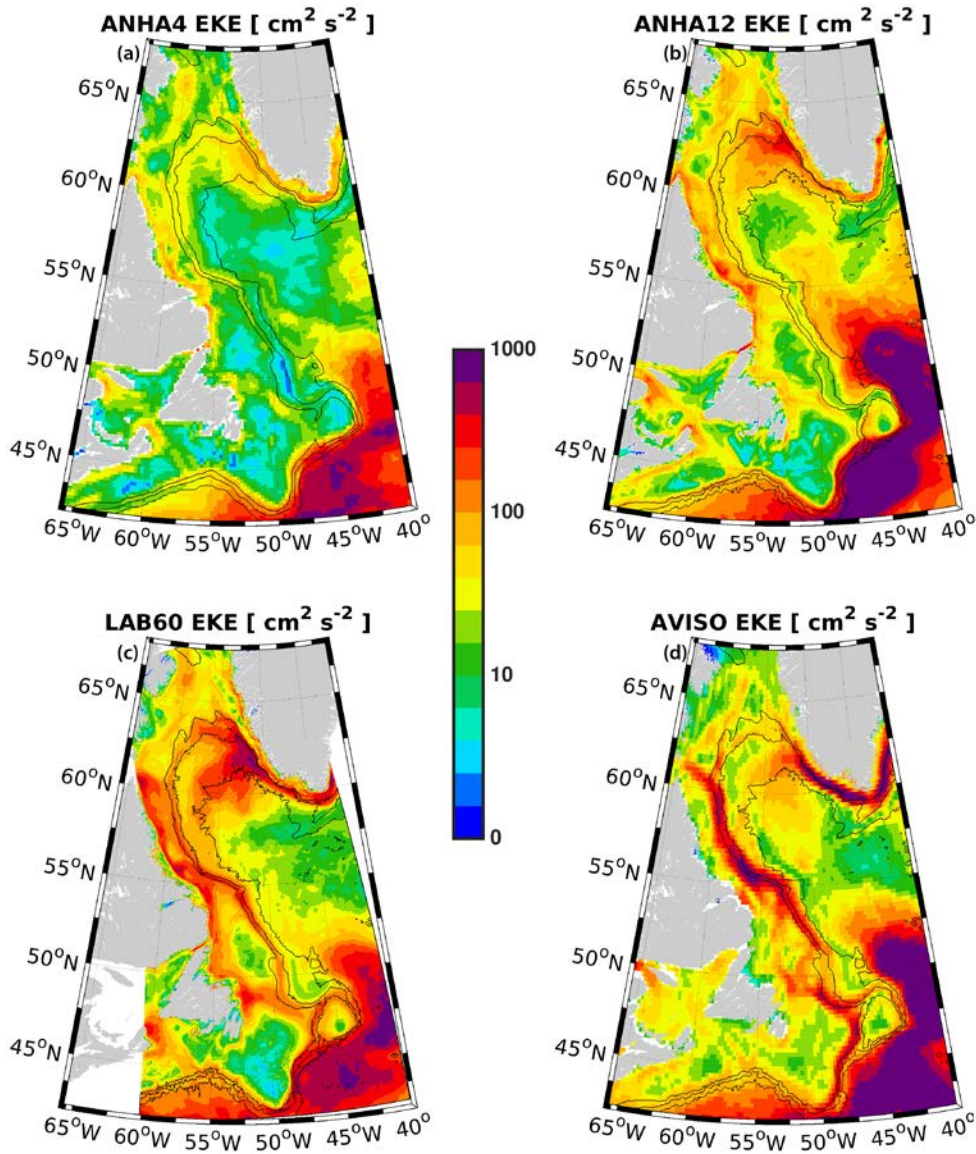
682

683

684

685

686

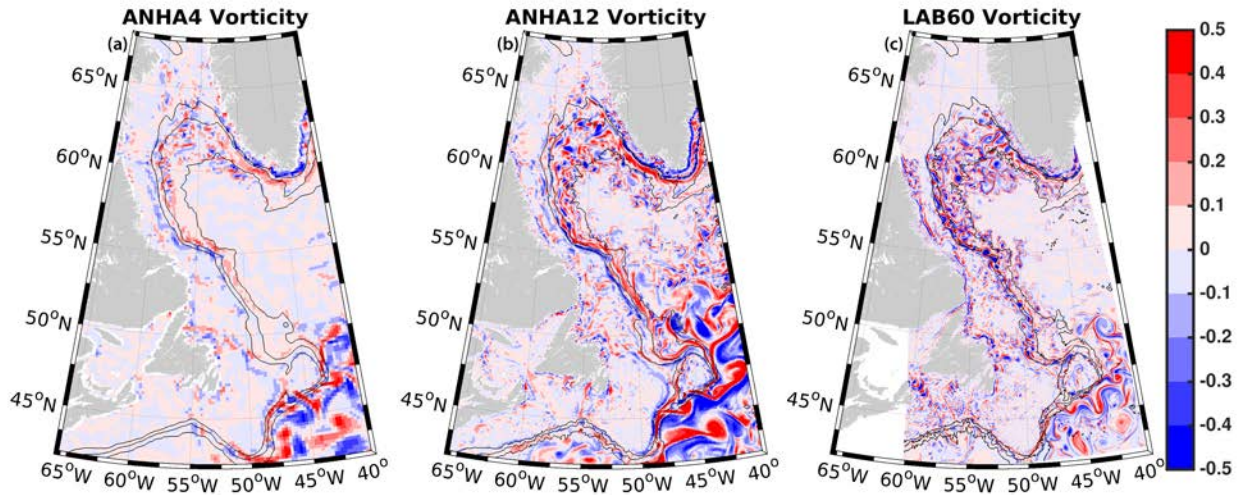


687

688 Figure 5: Eddy kinetic energy (EKE), as calculated from geostrophic velocities resulting from the
 689 sea level height anomaly, are shown for (a) ANHA4, (b) ANHA12, and (c) our LAB60 simulation,
 690 from 2004 to 2013. Observations via AVISO are identified in (d). The 1000m, 2000m, and 3000m
 691 isobaths are shown by the black contour lines. A log scale was used for clarity.

692

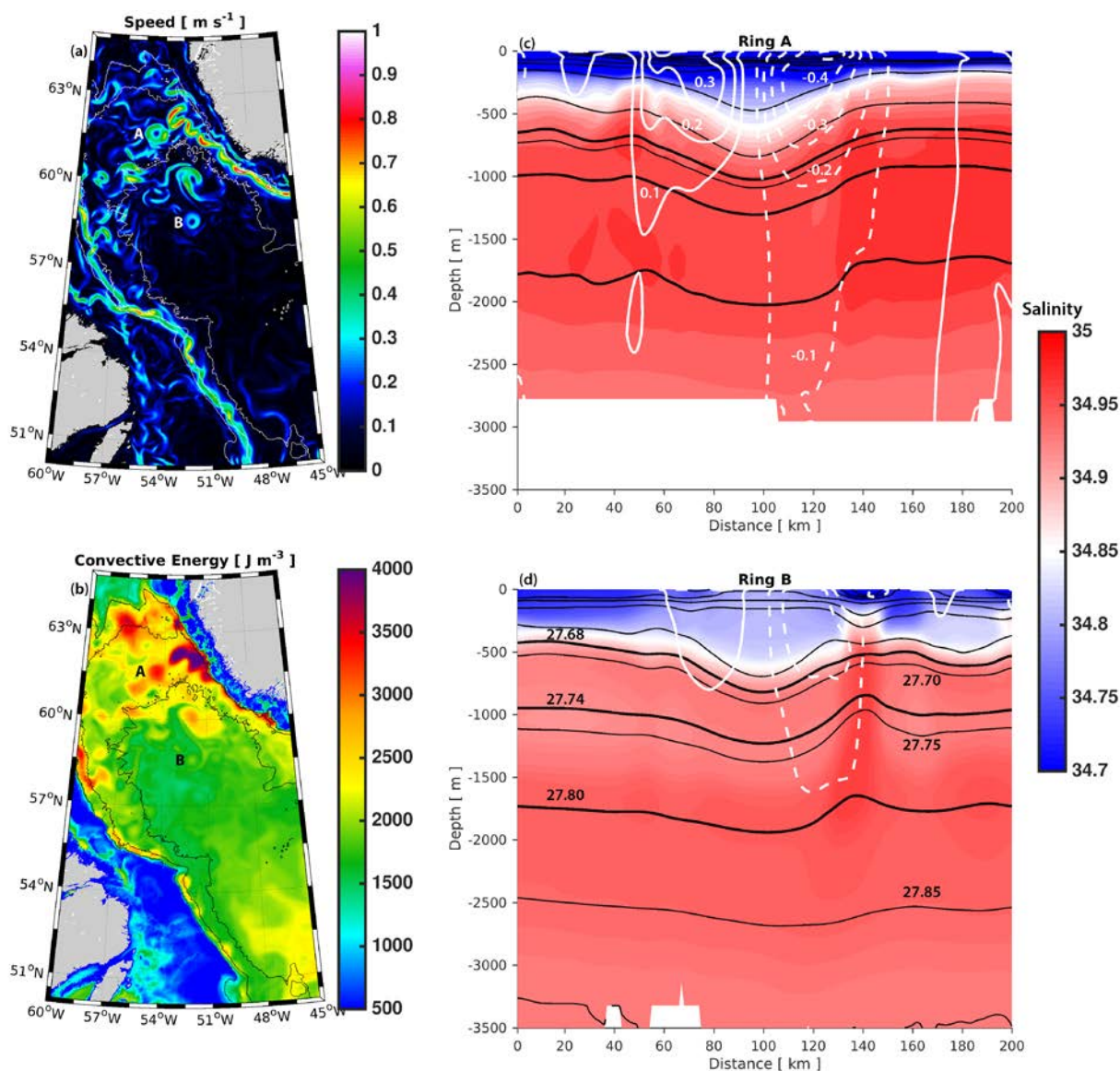
693



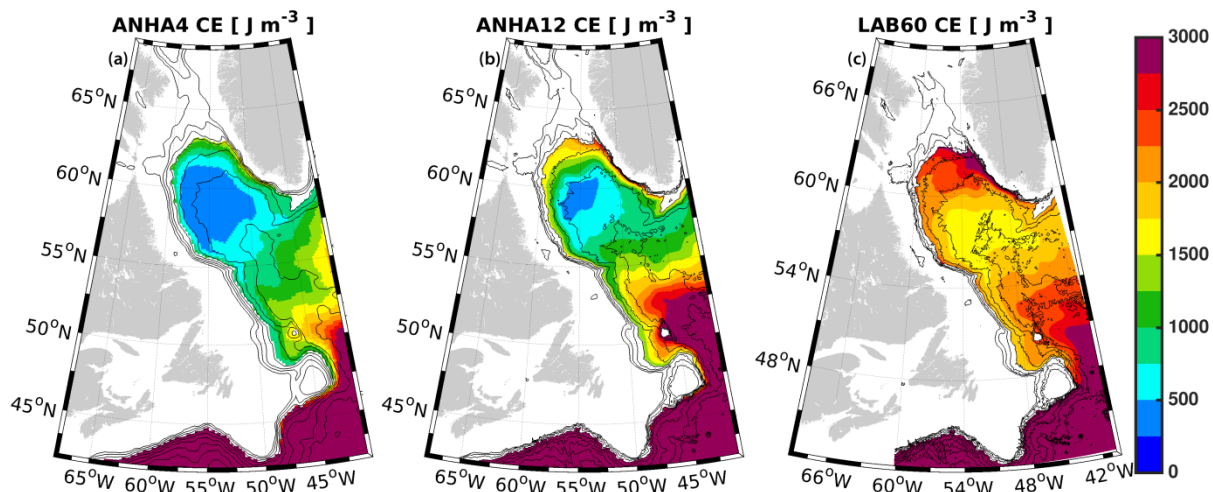
694

695 Figure 6: Top 50m relative vorticity, normalized by the planetary vorticity, as simulated by (a)
696 ANHA4, (b) ANHA12, and (c) LAB60 on 16 March 2008. The 1000m, 2000m, and 3000m isobaths
697 are shown by the black contour lines.

698

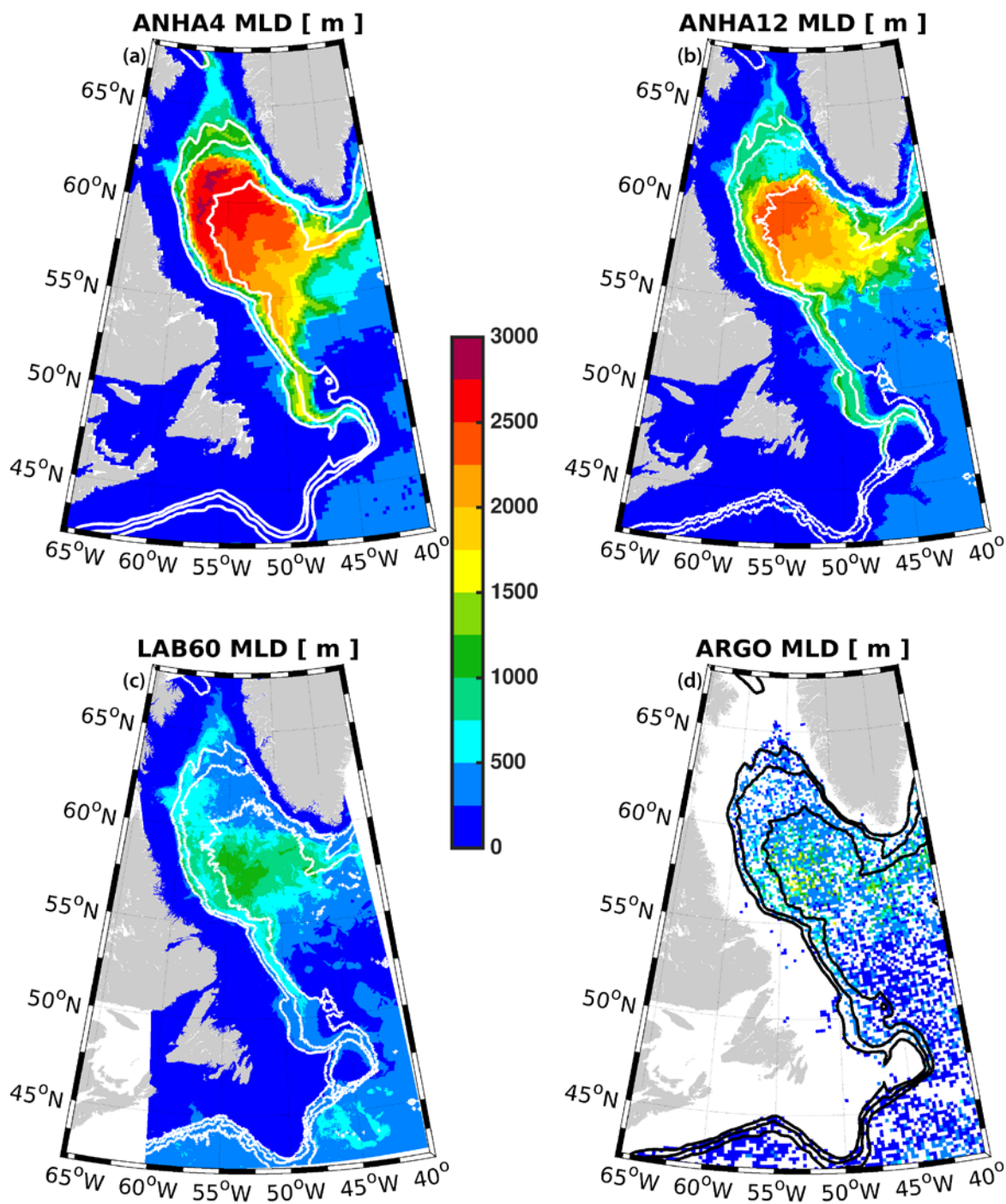


699
 700 Figure 7: LAB60 snapshot (26 July 2007) of the surface speed (a) and convective energy (b)
 701 within the Labrador Sea. Two Irminger Rings are identified by their age with letters: Ring A is a
 702 young Irminger Ring, while Ring B is comparatively older. An east-west cross section through
 703 each of these Irminger Rings is shown in (c) and (d) where colors indicate salinity, black
 704 contours indicate potential density using a contour interval of 0.05 kg m^{-3} , and white contours
 705 indicate meridional velocity where southern flow is dashed and northern flow is solid, using a
 706 contour interval of 0.1 m s^{-1} . Thick black contours indicate the potential density classification of
 707 Upper Labrador Sea Water ($\sigma_\theta = 27.68$ to 27.74 kg m^{-3}) and Classical Labrador Sea Water ($\sigma_\theta =$
 708 27.74 to 27.80 kg m^{-3}).



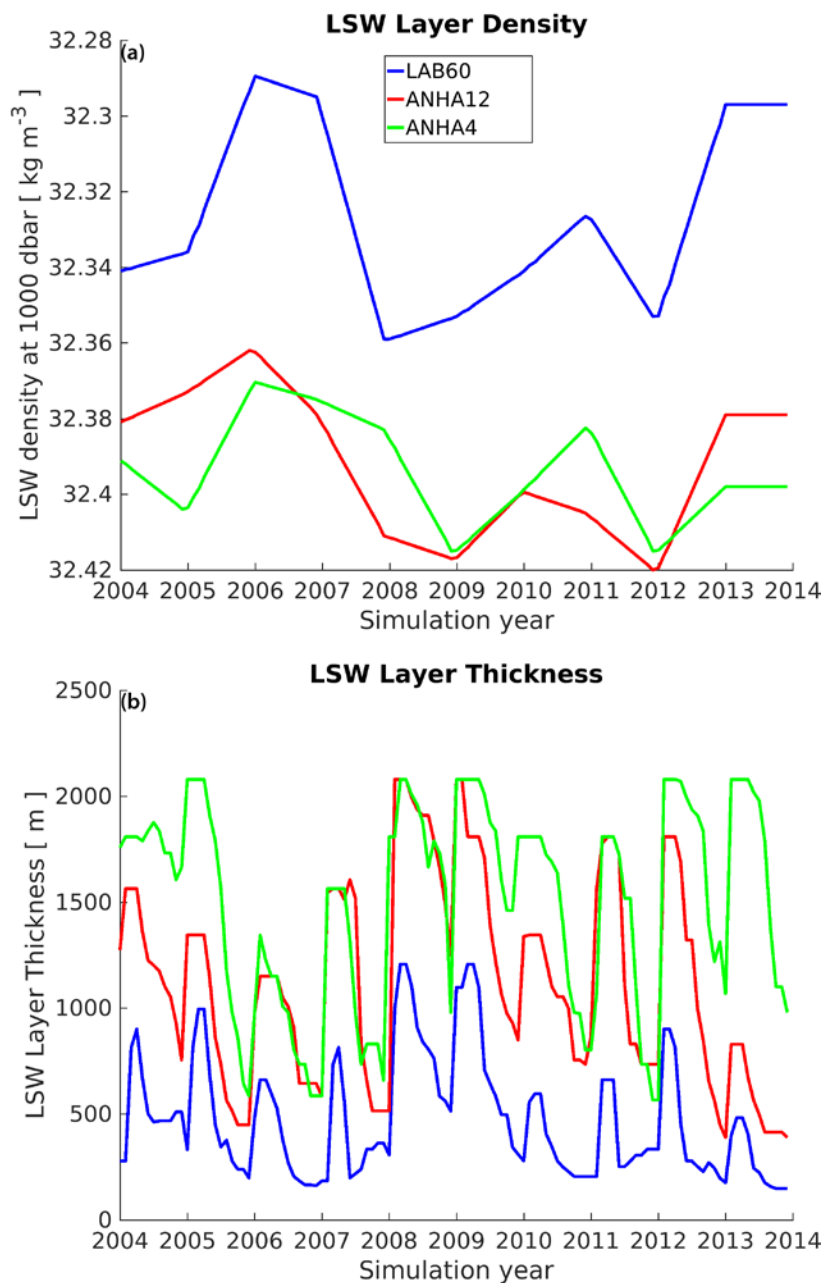
709

710 Figure 8: Convective energy (CE), the strength of stratification down to a reference depth of
 711 2000m, is shown for (a) ANHA4, (b) ANHA12, and (c) LAB60. Convective energy was averaged
 712 from 2004 through 2013. Values where the depth of the seafloor was less than 2000m were
 713 removed to preserve clarity. Bathymetric contours (black lines) are shown every 500m.



714
 715 Figure 9: Maximum mixed layer depth for (a) ANHA4, (b) ANHA12, (c) LAB60, as well as (d)
 716 ARGO observations, where available, from 2004 through the end of 2013. For clarity, the ARGO
 717 data were placed on the same grid as ANHA4. The 1000m, 2000m, and 3000m isobaths are
 718 shown via the white and black contours

719



720

721 Figure 10: Labrador Sea Water (LSW) density (a) and thickness (b) for the LAB60, ANHA12, and

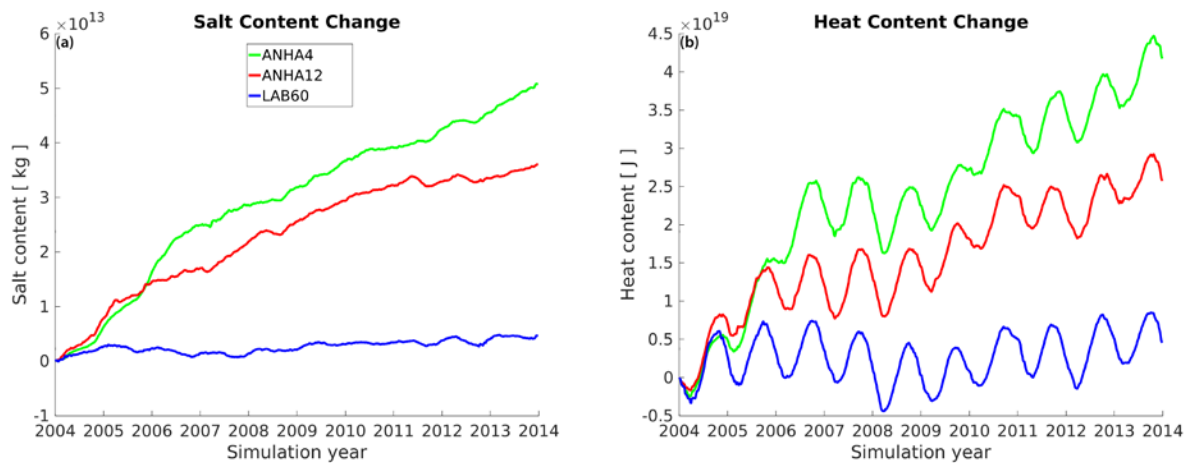
722 ANHA4 configurations. LSW density was determined from the thickest layer where a 0.001 kg

723 m⁻³ change in potential density (ref: 1000 dbar) occurred within the black polygon outlines in

724 Fig 1c. The LSW layer was then calculated between this density and one which was 0.02 kg m⁻³

725 less dense.

726



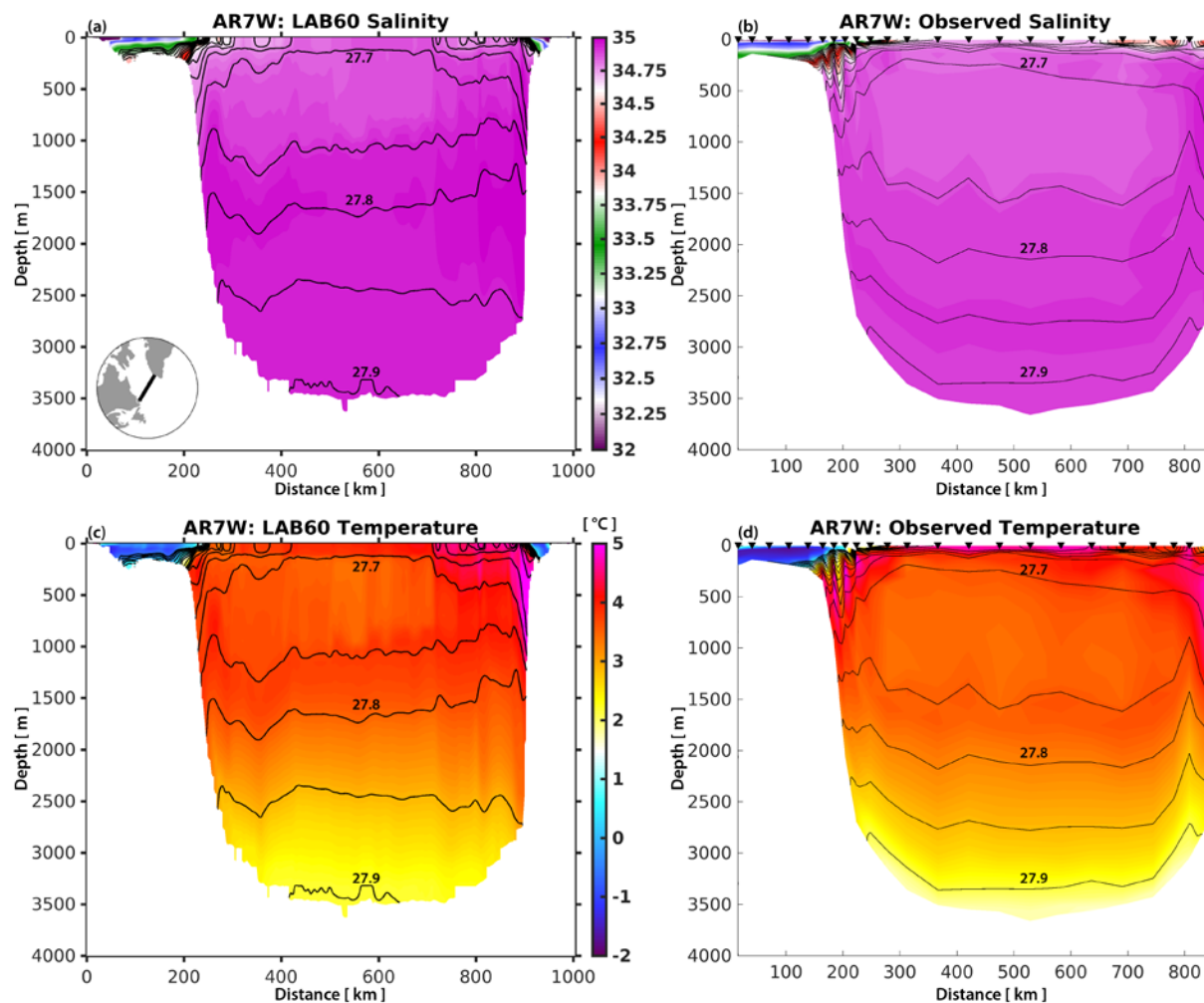
727

728 Figure 11: Numerical salt (a) and heat (b) drift in our three simulations as they evolve since 1

729 Jan 2004. Salt and heat content is calculated over the full ocean column within the polygon in

730 Fig. 1c.

731



732
 733 Figure 12: Salinity (top) and temperature (bottom) section across AR7W as determined by the
 734 LAB60 simulation (left) and observations (right) from May 2008. Downward triangles identify
 735 collection sites across the AR7W transit carried out by the CCGS Hudson. Potential density
 736 (black contours) isopycnal interval is 0.05 kg m^{-3} .